minerals

MDPI

Article

Study on Microstructure Evolution of Oolitic Hematite during Microwave Fluidization Roasting

Wentao Zhou, Yongqiang Zhao *, Xianjun Lyu, Wenhao Gao, Huili Su and Chuanming Li

College of Chemical and Biological Engineering, Shandong University of Science and Technology,
Qingdao 266590, China; zhouwentao@sdust.edu.cn (W.Z.); xianjun_lyu@sdust.edu.cn (X.L.);
gwh19991206@163.com (W.G.); xss19862855356@163.com (H.S.); lcm9810@163.com (C.L.)
* Correspondence: zhaoyq@sdust.edu.cn

Abstract: To explore the microstructure evolution of oolitic hematite during microwave fluidization roasting, COMSOL multiphysics and scanning electron microscopy (SEM)–energy-dispersive spectrometry (EDS) were used to simulate and explore the microstructure evolution. The simulation results indicated that with the extension of microwave heating time and the increase of microwave power, the surface temperature in the particle model progressively increased, and the heating rate of hematite was the fastest, followed by quartz and apatite; simultaneously, the temperature stress and difference between the three mineral interfaces in the model were increased. The SEM–EDS results illustrated that there were microcracks at the interface between iron minerals and gangue minerals, such as quartz and apatite, and the microcracks were more obvious at the interface between iron minerals and quartz minerals. With the extension of microwave treatment time, the microcracks were gradually extended and expanded inward along the outer edge of oolitic and gradually formed in the core of the oolitic structure. Appropriately increasing the roasting temperature, prolonging the roasting time, and increasing the CO concentration made the particle surface more loose and rough, and produced more cracks and pores, while the ore surface presented a honeycomb morphology.

Keywords: oolitic hematite; microwave roasting; simulation; microstructure evolution

check for updates

Citation: Zhou, W.; Zhao, Y.; Lyu, X.; Gao, W.; Su, H.; Li, C. Study on Microstructure Evolution of Oolitic Hematite during Microwave Fluidization Roasting. *Minerals* **2022**, *12*, 507. https://doi.org/10.3390/min12050507

Academic Editors: Josep Oliva and Hernan Anticoi

Received: 20 March 2022
Accepted: 18 April 2022
Published: 20 April 2022

Publisher's Note: MDPI stays neutral with regard to jurisdictional claims in published maps and institutional affiliations.

Copyright: © 2022 by the authors. Licensee MDPI, Basel, Switzerland. This article is an open access article distributed under the terms and conditions of the Creative Commons Attribution (CC BY) license (https://creativecommons.org/licenses/by/4.0/).

1. Introduction

Iron ore is a major strategic requirement for supporting the resources of China's iron and steel industry. Domestic iron ore production is struggling to meet the needs of the development of the iron and steel industry, because of its low grade, fine particle size, barely dissociated structure, and complex composition, resulting in the sustained growth of annual iron ore imports, which poses a great threat to the healthy and sustainable development of China's iron and steel industry, and even the national economy. In 2020, China's iron ore reserves stood at 85 billion tons, of which the oolitic hematite reserves were more than 10 billion tons [1,2]. Therefore, it is important to realize the efficient development and utilization of oolitic hematite resources and improve the self-sufficiency rate of iron ore.

Since the 1920s, France, Egypt, Canada, Israel, Saudi Arabia, and other countries have carried out abundant experimental research on oolitic hematite; however, the overall beneficiation effect was unsatisfactory. For instance, the French Ferrous Metallurgy Research Institute adopted the dry high-intensity magnetic separation process to treat oolitic hematite and achieved a separation index of concentrate with an iron grade of 40% and recovery rate of 86%. As foreign countries possessed high-grade iron ore resources, the research on the beneficiation of complex refractory iron ore has become basically stagnant in recent years. Simultaneously, China's scientific researchers have carried out extensive research work on the efficient utilization of oolitic hematite ore and made important progress. The research methods can be divided into physical beneficiation processes, leaching processes, direct reduction magnetic separation processes, and magnetization roasting [3–8]. The iron grade of concentrate obtained by conventional beneficiation methods, such as single flotation and selective flocculation reverse flotation, are usually about 56%, with the iron recovery being about 50–70% [8]. Significant dephosphorization effects can be achieved by bioleaching and acid leaching; however, microorganisms must be collected, separated, cultivated, and domesticated in the process of microbial leaching, resulting in a long leaching time and low production efficiency. The acid leaching process contains some disadvantages, including a high acid consumption, a corrosion of equipment, and serious pollution. The above problems limit the large-scale application of leaching processes in the iron ore industry [9]. A high separation effect can be obtained by using direct reduction and magnetic separation processes to treat oolitic hematite ore; however, due to the low iron grade of ore and a complex process flow, a high energy consumption and high cost are generated in the application of the process.

Focusing on the efficient development and utilization of complex refractory iron ore resources, many scholars have proven that magnetization roasting with magnetic separation technology is one of the most effective means to deal with refractory iron ore in long-term practice [10–12]. For the magnetization roasting of complex refractory iron ores, scholars have successively developed a variety of magnetization roasting technologies and equipment, such as shaft furnace roasting, rotary kiln roasting, microwave roasting, and suspension roasting. Conversely, fluidization magnetization roasting technology has exhibited considerable promise for use in the treatment of refractory iron ore, because of its high product stability, favorable heat and mass transfer effects, and high level of automation [13]. However, fluidization magnetization roasting technology has the problems of environmental pollution and substantial energy consumption, making it infeasible, owing to its inability to satisfy the "clean and green" standards of the steel industry [14,15]. Microwave roasting has the advantages of selective heating, a catalytic chemical reaction, environmental protection, high efficiency, and no pollution. If the microwave roasting process can overcome the barriers of equipment amplification, it has broad development prospects. Therefore, based on the technical concept of "microwave heating combined with fluidization magnetization roasting for the treatment of refractory iron ore", that is, making full use of the advantages of high-efficiency heat and mass transfer of fluidization roasting and microwave selective rapid heating, the authors put forward a new technology of microwave fluidization roasting. Under optimized conditions, a magnetic separation concentrate with an iron grade of 58.7% and recovery rate of 89.3% could be obtained by the new process [14]. Compared with the traditional process, the iron grade was increased by 1.84 percentage points, and the recovery rate was increased by 0.63 percentage points. However, the microstructural evolution of oolitic hematite ore during microwave fluidization roasting was not clear. Therefore, this paper used COMSOL multiphysics software to explore the temperature distribution and stress distribution of oolitic hematite ore particles in a microwave field. On this basis, the microstructural evolution of oolitic hematite particles during microwave fluidization roasting was studied by means of SEM–EDS.

2. Materials and Methods

2.1. Materials

The oolitic hematite ore used in the test was provided by Liuzhou Iron and Steel Group. The ore sample was crushed, screened, mixed, and shrunk as the raw material for the test. The chemical multi-element analysis of raw materials was carried out using X-ray fluorescence (XRF), and the results are presented in Table 1. As indicated by Table 1, the main useful element in the ore was 46.70% iron; the main impurity components were SiO_2 and Al_2O_3, with contents of 19.17% and 5.71%, respectively; while, the harmful substances P_2O_5 was present at a concentration of 2.34%.

Table 1. The chemical composition of oolitic iron ore (mass %).

Component	TFe	FeO	P_2O_5	SiO_2	Al_2O_3	CaO	MgO	K_2O	Na_2O	LOI
Content	46.70	2.43	2.34	19.17	5.71	2.45	0.30	0.63	0.18	4.25

To find out the types of minerals in the raw materials, the mineral phase of the ore was qualitatively analyzed using an X-ray diffractometer (XRD). As shown in Figure 1, the main minerals in the ore were hematite, quartz, apatite, kaolinite, and chlorite. Due to the low content of other minerals, they could not be displayed in the XRD spectrum. The embedding characteristics of the main minerals in the ore were studied by optical microscope. As shown in Figure 2, hematite, quartz, apatite, and other minerals in the ore were closely embedded with each other, and a mineral was wrapped around each other to form an oolitic structure with a concentric layered structure.

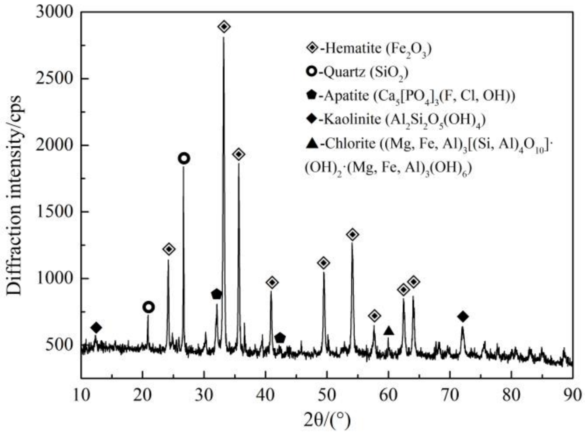

Figure 1. XRD pattern of oolitic iron ore.

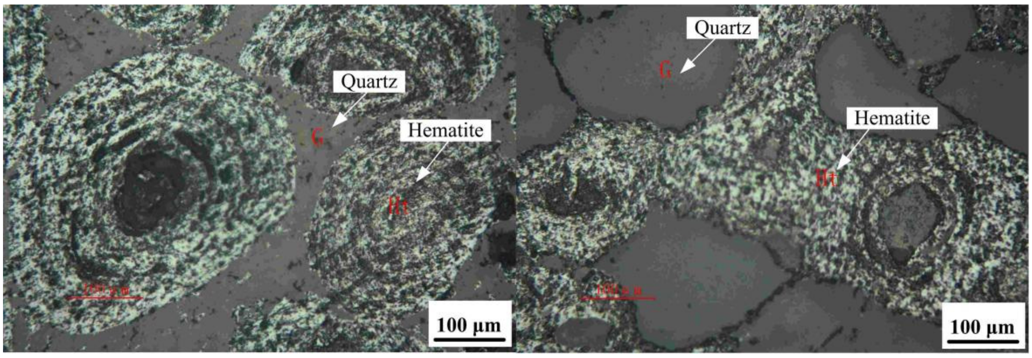

Figure 2. Optical microscope photos of the main minerals in the ore.

2.2. Methods and Equipment

2.2.1. Analytical Methods

X-ray diffraction (XRD), especially powder X-ray diffraction, plays an important role in the study of mineral crystallization process and phase transformation, mineral phase, mineral defects, and mineral crystal structure. In this experiment, powder X-ray diffraction detection technology was used to analyze the phase of the raw material. The detection instrument used was a pw3040 X-ray diffractometer produced by Panalytical B. V in the Netherlands. The working parameters were the following: Cu target radiation, nickel filter, solid detector, scanning range of $2\theta = 5~90°$, tube voltage 40 kV, tube current 40 Ma, step scanning, step size 0.033°, residence time of each step 20.68 s, incoming ray wavelength 0.1541 nm, scanning speed $12°\cdot min^{-1}$, and working temperature 298 K. The specific operations were as follows: The mass of raw materials was required to be about 3 g, then they were ground with mortar to a particle size of −0.074 mm. The ground sample was pressed. During the pressing process, the surface of the sample should be flat and uniform, and no obvious particles should be seen. After the sample was pressed, it was put into the XRD equipment to start detection. A scanning electron microscope could then be used to observe the micro morphology and dispersion state of the materials, with the advantages of high magnification, clear image, and simple operation. In this test, a TESCAN MIRA3 field emission scanning electron microscope system, produced by Tisken, Czech Republic, and equipped with a new uitim maxn silicon drift energy spectrometer (EDS) and Nordiys Max3 electron backscatter diffraction analysis system (EBSN) from Oxford Instrument, UK, were used to characterize the micro morphology and corresponding micro area components of the test samples. The specific operations were as follows: an appropriate amount of test samples were prepared, inlaid, fixed with epoxy resin, and then polish. Then, the polished sample surface was sprayed with gold using a vacuum coating instrument, and finally the SEM sample was prepared. The sample to be tested was fixed on the sample table with conductive tape, the microstructure was observed using a scanning electron microscope, and the microstructure of the different areas was analyzed with an EDS energy spectrum. The main parameters of electron microscope system were as follows: a field emission electron gun, a maximum theoretical magnification of 1 million times, SEM image resolution of 1.0 nm and 30 kV, EDS probe of silicon drift detector, and a spatial resolution and angular resolution of ebsn of 0.1 µm and 0.5 µm.

2.2.2. Roasting Test Method

An independently designed and manufactured microwave fluidization roasting furnace was used as the main equipment in the test. A schematic diagram of the equipment is shown in Figure 3a. The roasting furnace was composed of the furnace body, atmosphere system, insulation system, microwave system, cooling system, temperature measurement system, control system, and cabinet. It possessed the characteristics of rapid heating, high automation level, being energy saving and efficiency, convenient operation, and accurate temperature control. The microwave fluidization roasting system (Figure 3b) was composed of a gas mixing supply device, fluidized bed, temperature control and transmission device (accuracy ±2 °C), and microwave cavity device. The gas flow range of the gas mixing supply device was 0~1000 mL/min. Different gases could be input according to the test needs, and then the roasting test could be carried out in different atmospheres. Through the gas mixing supply device, the fluidizing medium entered the breathable quartz plate fluidized bed (diameter Ø20 mm) from the bottom channel of a specially-shaped quartz tube, and fully contacted the materials placed on the quartz plate. By adjusting the gas flow, the material particles were in a suspended state on the quartz plate. The microwaves radiated the material in the fluidized bed through the cavity, to heat it to a predetermined temperature, and the tail gas was discharged to the tail gas treatment device through the top of the specially-shaped quartz tube.

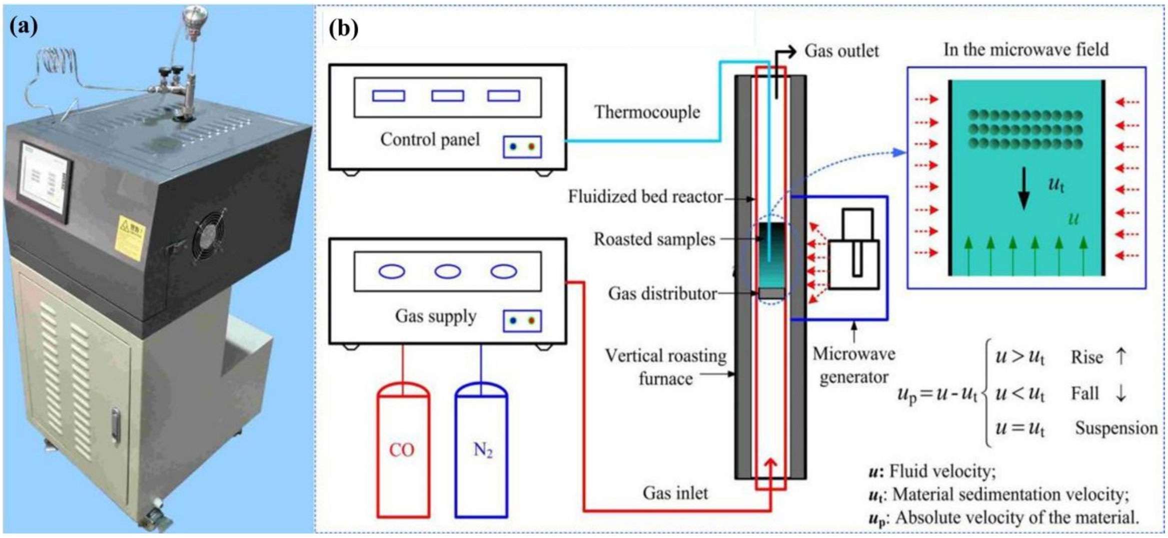

Figure 3. Schematic diagram of the microwave fluidization roasting system: (**a**) Diagram of the equipment, (**b**) schematic diagram of the microwave fluidization roasting system.

For the microwave fluidization roasting process of coarse particles (−0.425 + 0.15 mm), the test steps were as follows: take an appropriate mass of test samples (12 g) and place them in a roasting tube, place the roasting tube in the microwave fluidization roasting furnace, and introduce 250 mL/min N_2. Set the microwave power to 1300 W in the heating stage, set the microwave power adjustment range to 500–600 W in the constant temperature stage, and set the microwave treatment temperature and time. Turn on microwave heating and start timing when the treatment temperature reaches the set value. After reaching the predetermined processing time, turn off the microwave immediately, pour the materials in the roasting tube into the basin and cool the air to room temperature to obtain the microwave treated sample. For the microwave fluidization roasting process of fine particles (−0.15 mm), the test steps were as follows: take an appropriate mass of test samples (12 g) and place them in a roasting tube, place the roasting tube in the microwave fluidization roasting furnace, and vent the air in the tube with 250 mL/min N_2. Set the microwave roasting temperature and time. Turn on the microwave heating. When the microwave roasting temperature reaches the predetermined value, start to introduce an appropriate amount of CO (the total gas volume of CO and N_2 is 700 mL/min, and the concentration of CO is the volume fraction of the total gas), and start to calculate the roasting time. After reaching the predetermined roasting time, immediately stop the feeding of CO, continue to feed N_2, and turn off the microwave at the same time. Take out the roasting tube and cool it to room temperature in N_2 atmosphere, pour out the roasted products, and the roasting test is completed.

2.2.3. Simulation Method

COMSOL multiphysics is a large-scale analysis software based on the finite element method, which simulates real physical phenomena by solving partial differential equations. Owing to the different properties of the main minerals in oolitic hematite ore, the temperature rise characteristics of different minerals show great differences in the process of microwave heating. The temperature distribution and stress distribution of oolitic hematite particles in a microwave field were studied using the heat transfer module and structural mechanics module in the COMSOL multiphysics software. In the multi-field coupling of temperature field, microwave field, and stress field, the temperature distribution and stress distribution model of oolitic hematite particles can be described using Maxwell equations. According to the structural characteristics and mineral composition of oolitic hematite ore, and to more conveniently and clearly characterize the ore particles, this paper simplified the single oolitic particle into a spherical structure. According to the size of the main mineral components contained in the ore, the ore contained hematite, quartz, and apatite, from the inner layer to the outer layer. A model view is presented in Figure 4. According to the data in the software and the data consulted, the mineral physical parameters used in the simulation are shown in Table 2 [16,17].

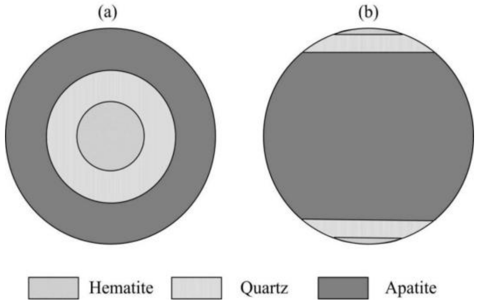

Figure 4. Schematic diagram of the mineral composition of oolitic ore: (**a**) top view; (**b**) front view.

Table 2. Physical parameters of simulated materials.

Physical Parameters	Quartz	Hematite	Apatite	Unit
Relative dielectric constant	4.20	25.00	5.72	1
Thermal conductivity	3.00	12.00	1.44	W/mK
Density	2650.00	4980.00	3200.00	kg/m^3
Constant pressure heat capacity	820.00	648.00	832.00	J/kg·°C
Conductivity	10^{-12}	10^{-2}	10^{-11}	S/m
Relative permeability	1.00	1.05	1.00	1
Young's modulus	382.76	209.08	600.00	GPa
Poisson's ratio	0.08	0.25	0.25	1
Coefficient of thermal expansion	0.55	9.60	8.90	10^{-6}/°C

3. Results and Discussion

3.1. Simulation Result

3.1.1. Effect of Microwave Time on the Temperature and Stress Distribution of the Model

The temperature distribution and temperature stress distribution of the oolitic particle model were satisfied under the condition of a microwave power of 1000 W when the microwave heating time was 60 s, 90 s, 120 s, 200 s, and 300 s respectively. The results are shown in Figures 5 and 6, respectively.

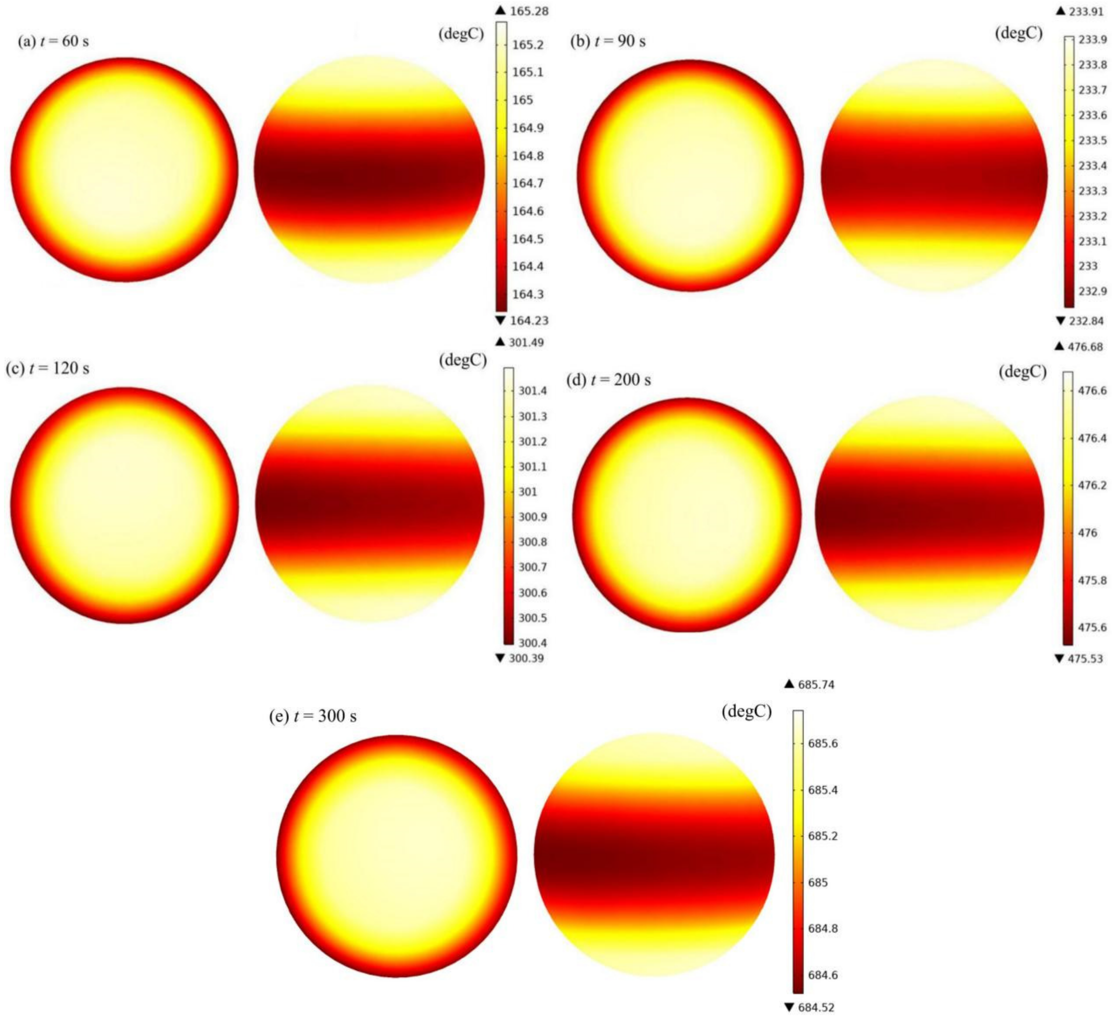

Figure 5. Temperature distribution of oolitic particle model with different microwave heating times and a microwave power of 1000 W: (**a**) 60 s, (**b**) 90 s, (**c**) 120 s, (**d**) 200 s, (**e**) 300 s.

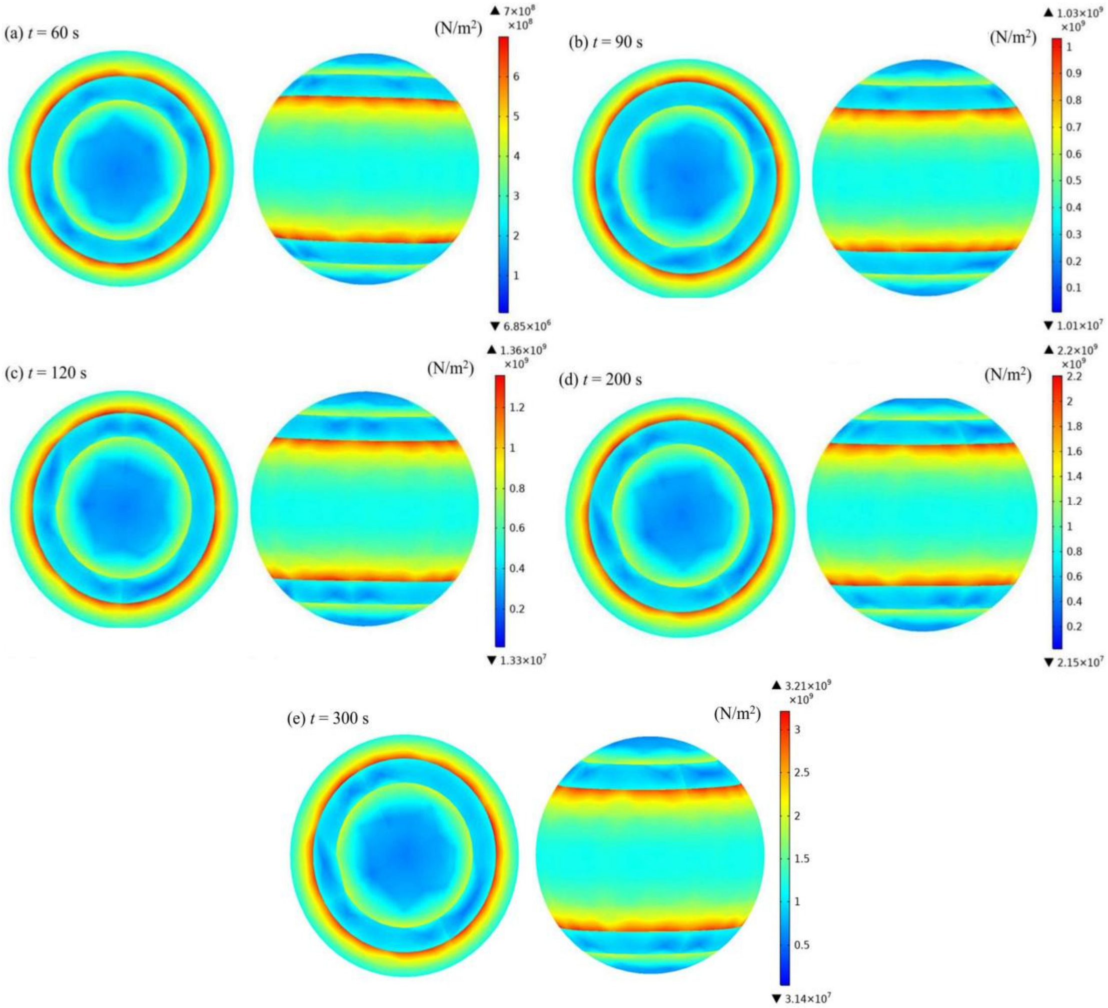

Figure 6. Temperature stress distribution of oolitic particle model with different microwave heating times and a microwave power of 1000 W: (**a**) 60 s, (**b**) 90 s, (**c**) 120 s, (**d**) 200 s, (**e**) 300 s.

As presented in Figures 5 and 6, with the extension of heating time, the maximum temperature and minimum temperature of the particle model surface gradually increased, indicating that the overall temperature of the model surface was increasing. At the same heating time, the temperature in the distribution area of hematite, quartz, and apatite was significantly different. The order of temperature levels was hematite > quartz > apatite, indicating that hematite had the strongest microwave absorption ability, followed by quartz and apatite. Simultaneously, with the extension of heating time, the surface temperature stress of the particle model also increased gradually. When the microwave heating time increased from 60 s to 300 s, the maximum stress on the particle surface increased from 7.0×10^8 N/m^2 to 3.2×10^9 N/m^2. With the same heating time, the regional temperature stress of hematite, quartz, and apatite was quite different, and the stress distribution between the acting mineral interfaces was more concentrated and the value was larger, which was mainly due to the differences in dielectric properties, thermal conductivity, and thermal expansion between different minerals, resulting in the formation of a temperature gradient at the mineral interface, and then the formation of temperature stress. Therefore, the temperature stress between the mineral interfaces increased gradually with the extension of microwave heating time.

3.1.2. Effect of Microwave Power on the Temperature and Stress Distribution of the Model

Under the condition of a microwave heating time of 120 s, the temperature distribution and temperature stress distribution of the oolitic particle model at microwave powers of 300 W, 500 W, 700 W, 900 W, and 1100 W were investigated. The results are shown in Figures 7 and 8.

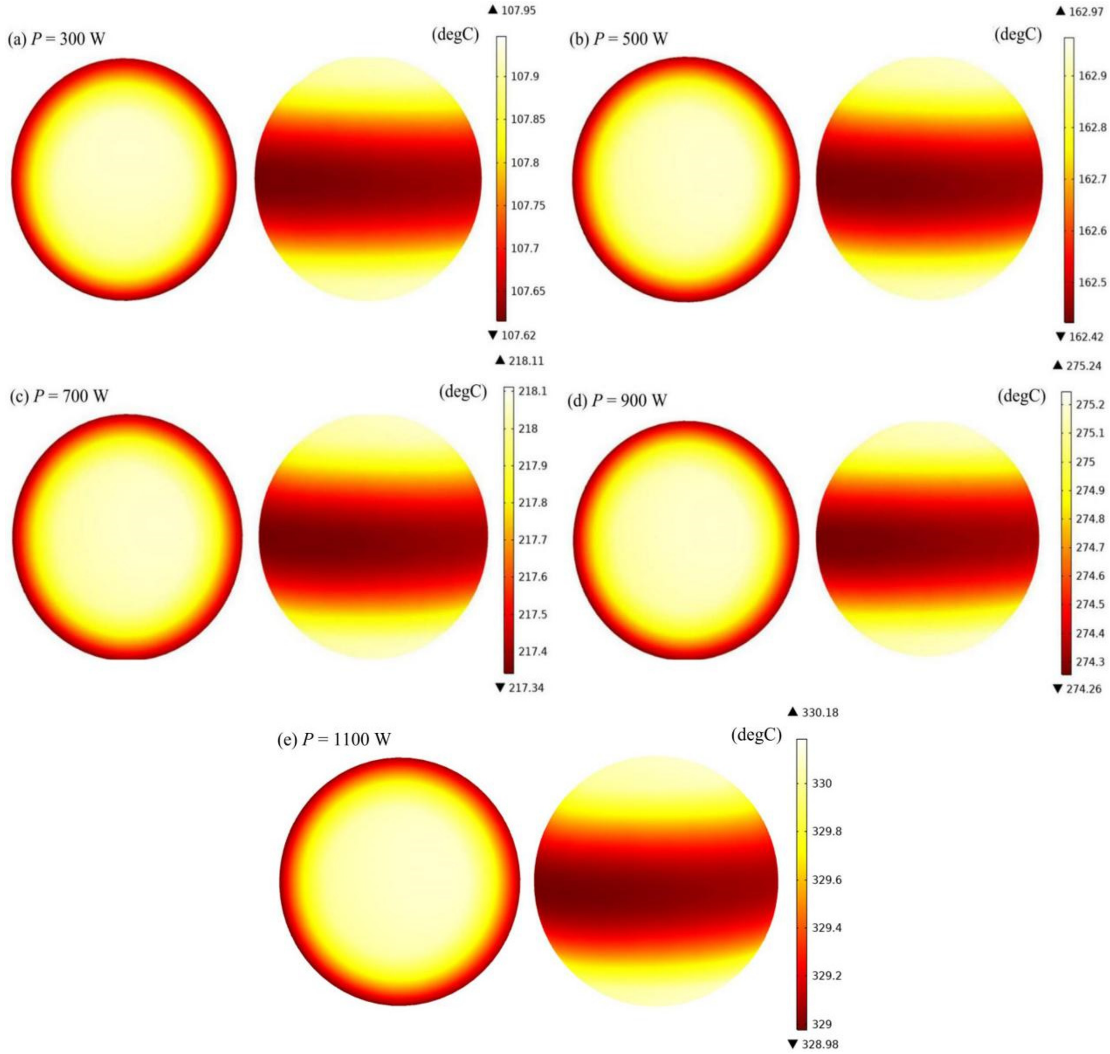

Figure 7. Temperature distribution of the oolitic particle model under different microwave powers, with a microwave heating time of 120 s: (**a**) 300 W, (**b**) 500 W, (**c**) 700 W, (**d**) 900 W, (**e**) 1100 W.

As shown in Figures 7 and 8, with the increase of microwave power, the microwave power density also increased, resulting in a continuous increase of the overall surface temperature of the model. Under the same microwave power, there were significant differences in the temperature distribution of the three mineral regions. The brightness of the hematite region was significantly stronger than that of quartz and apatite, indicating that the heating rate of hematite was the fastest, followed by quartz and apatite. Simultaneously, with the increase of microwave power, the temperature stress and stress difference between the three mineral interfaces in the model (the difference between the maximum stress and the minimum stress on the particle surface under the same microwave power) continued to increase. The maximum temperature stress increased from 4.2×10^8 N/m^2 (microwave power of 300 W) to 1.5×10^9 N/m^2 (microwave power of 1100 W), and the corresponding stress difference increased from 4.19×10^8 N/m^2 to 1.49×10^9 N/m^2.

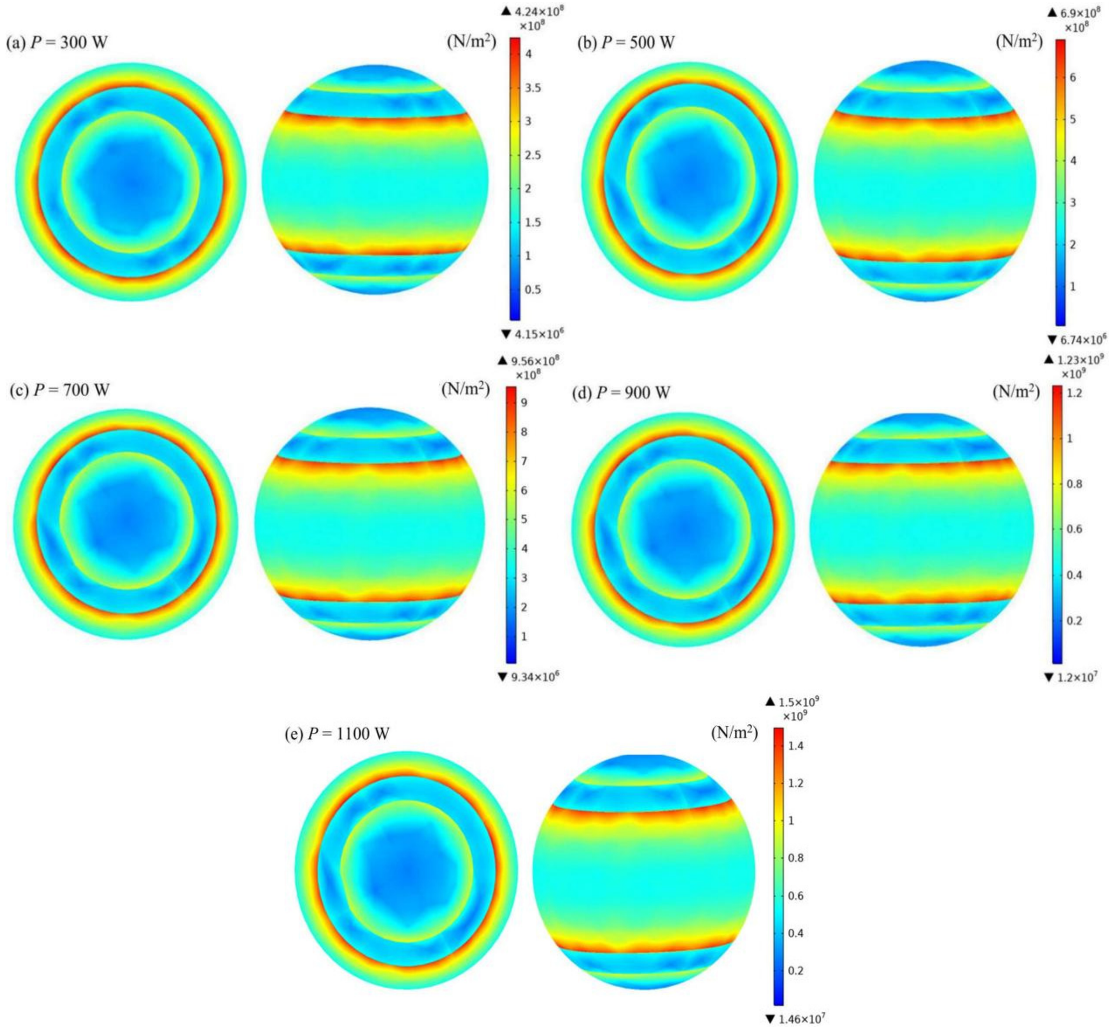

Figure 8. Temperature stress distribution of the oolitic particle model under different microwave powers, with a microwave heating time of 120 s: (**a**) 300 W, (**b**) 500 W, (**c**) 700 W, (**d**) 900 W, (**e**) 1100 W.

3.2. Microstructure Evolution

To explore the effect of microwave roasting on the microstructure of the ore, the morphology of the internal microstructure (−0.425 + 0.15 mm material) and surface microstructure (−0.15 mm material) of ore under different roasting conditions were analyzed. The roasted products were obtained under the conditions of a roasting temperature of 650 °C and roasting times of 2 min, 3 min, 4 min, and 5 min, respectively. The internal microstructure of the products was analyzed using SEM–EDS. the results are shown in Figure 9. Under different roasting temperatures (550 °C, 600 °C, and 650 °C), roasting times (3 min, 4 min, and 5 min), and CO concentrations (15%, 25%, and 35%), the surface micro morphology of the roasted products is shown in Figures 10–12, respectively.

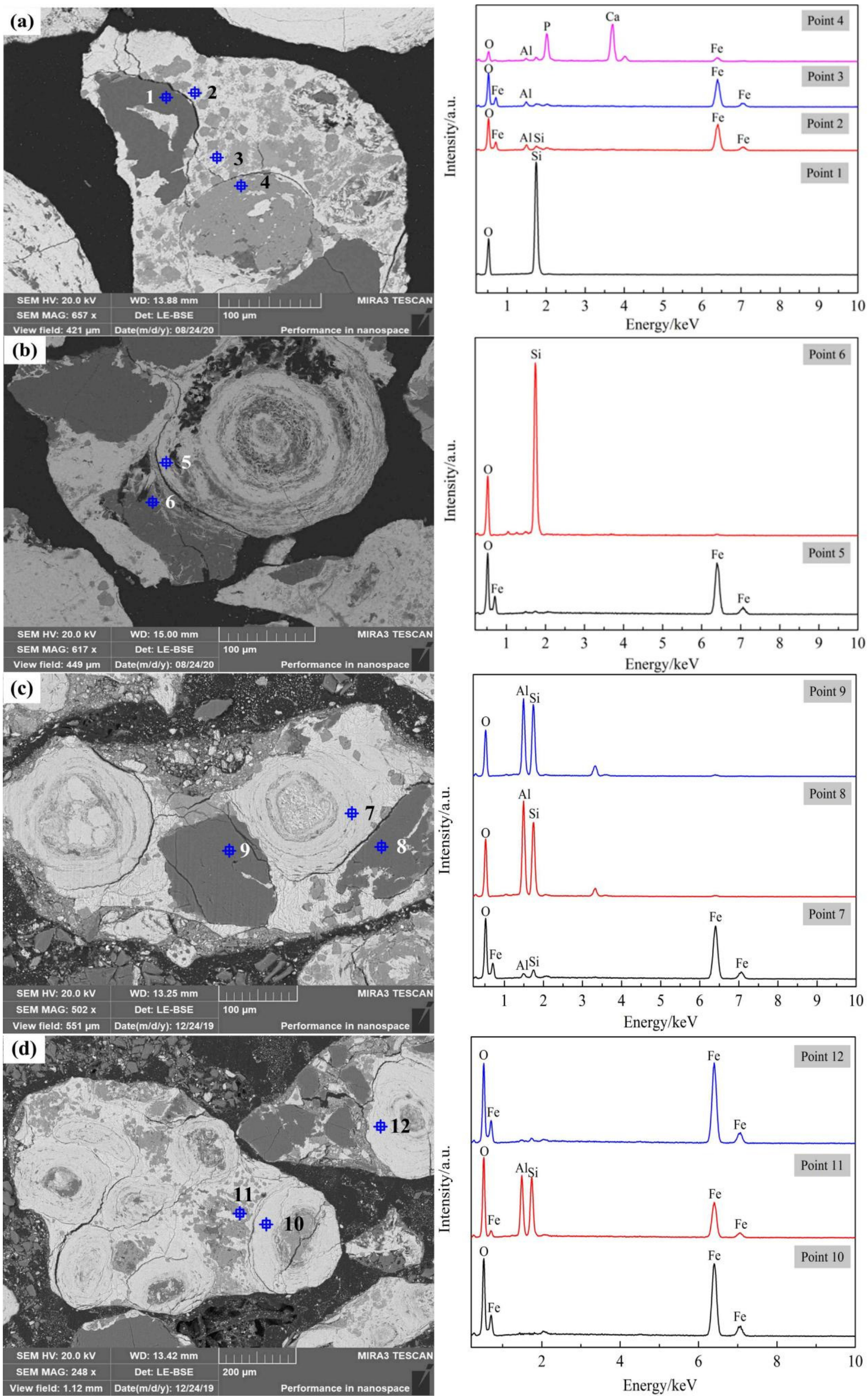

Figure 9. SEM images and EDS spectra of products with different roasting times, and with a roasting temperature of 650 °C: (**a**) 2 min, (**b**) 3 min, (**c**) 4 min, (**d**) 5 min.

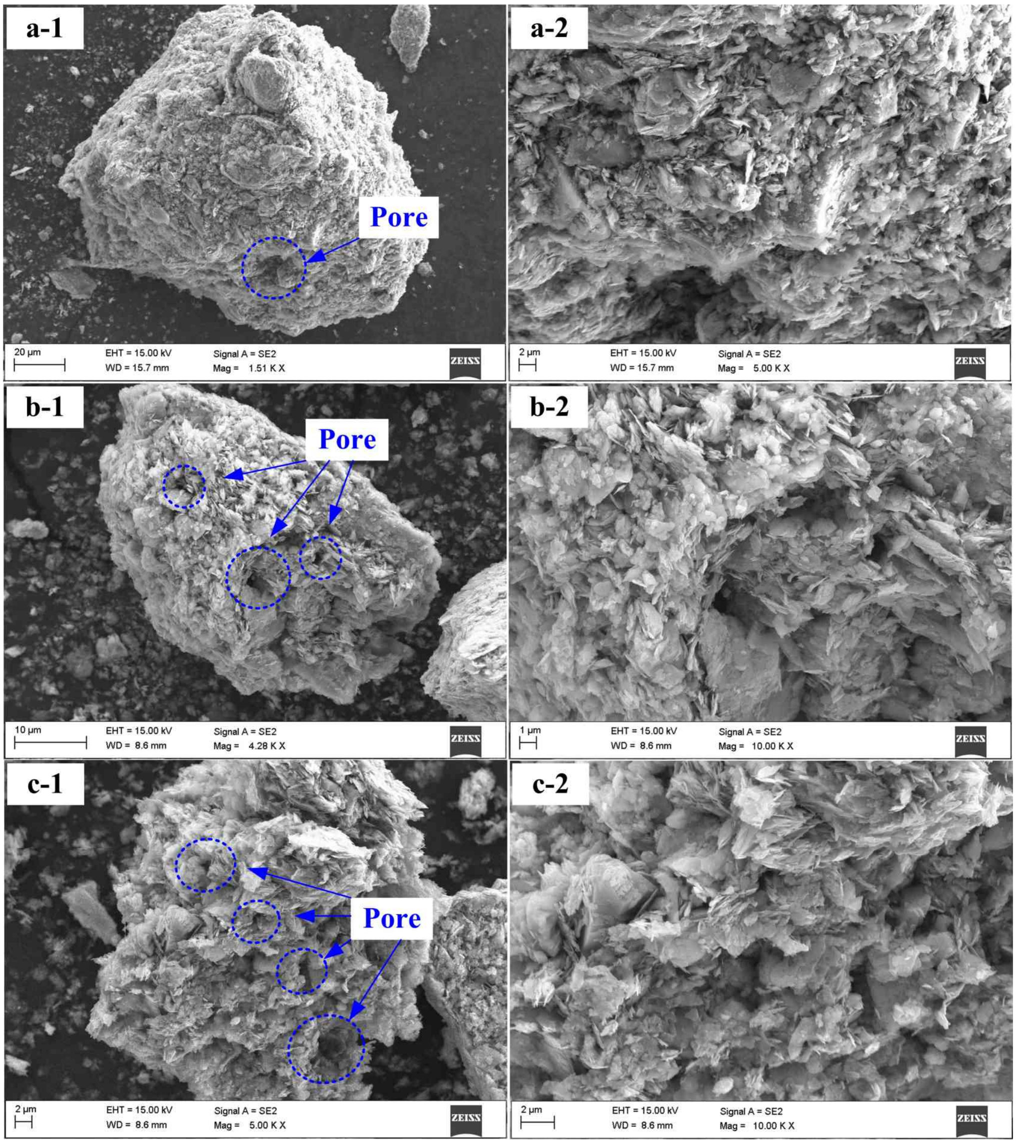

Figure 10. SEM images of materials at different roasting temperatures, with a CO concentration of 35% and roasting time of 5 min: (**a-1**,**a-2**) 550 °C, (**b-1**,**b-2**) 600 °C, (**c-1**,**c-2**) 650 °C.

As shown in Figure 9a, compared with the SEM images of raw ore (Figure 2), when the microwave time was 2 min, there were microcracks at the color boundary of the ore profile, and there were microcracks at the outer edge of oolite. According to the EDS calculation and analysis, the constituent elements of the point 1 area were Si and O, and this area was composed of quartz. The constituent elements in the point 2 area and point 3 area were Fe, O, and trace Si and Al, and this area was composed of iron mineral and trace aluminosilicate. The constituent elements in the point 4 region were Ca, P, O, and trace Fe and Al, and this region was mainly composed of apatite. The above results showed that when the microwave time was 2 min, there were microcracks between the interface of iron minerals and quartz, and apatite minerals, and the microcracks between the interface of iron minerals and quartz minerals were more obvious. As shown in Figure 9b, there were microcracks at the outer edge of oolite. According to the EDS calculation and analysis, the constituent elements in the point 5 area were Fe and O, and this area was composed of iron minerals. The constituent elements of the point 6 area were Si and O, and the area was composed of quartz. The above results show that there were microcracks at the interface between iron minerals and quartz minerals when the microwave time was 3 min. According to 9c, compared with the SEM images with microwave times of 2 min and

3 min, when the microwave time was 4 min, the microcracks at the color boundary of the ore profile were gradually widened. According to the EDS calculation and analysis, the point 7 area was mainly composed of Al, Si, O, and Fe, and this area was mainly composed of aluminosilicate and iron minerals. The constituent elements of point 8 were Fe and O, and this area was iron mineral. The point 9 area was mainly composed of Al, Si, and O, which was aluminosilicate. The above results indicated that there were microcracks at the interface between iron minerals and aluminosilicate minerals when the microwave time was 4 min. As shown in Figure 9d, and compared with the SEM image when the microwave time was 4 min, the microcracks at the color boundary of the ore profile gradually extended inward when the microwave time was 5 min; and it was found that the oolitic structure core also began to form microcracks. According to the EDS calculation and analysis, the constituent elements of points 10 and 12 were Fe and O, and this area was composed of iron mineral. Point 11 was mainly composed of Al, Si, Fe, and O, this area was composed of a mixture of aluminosilicate and iron minerals.

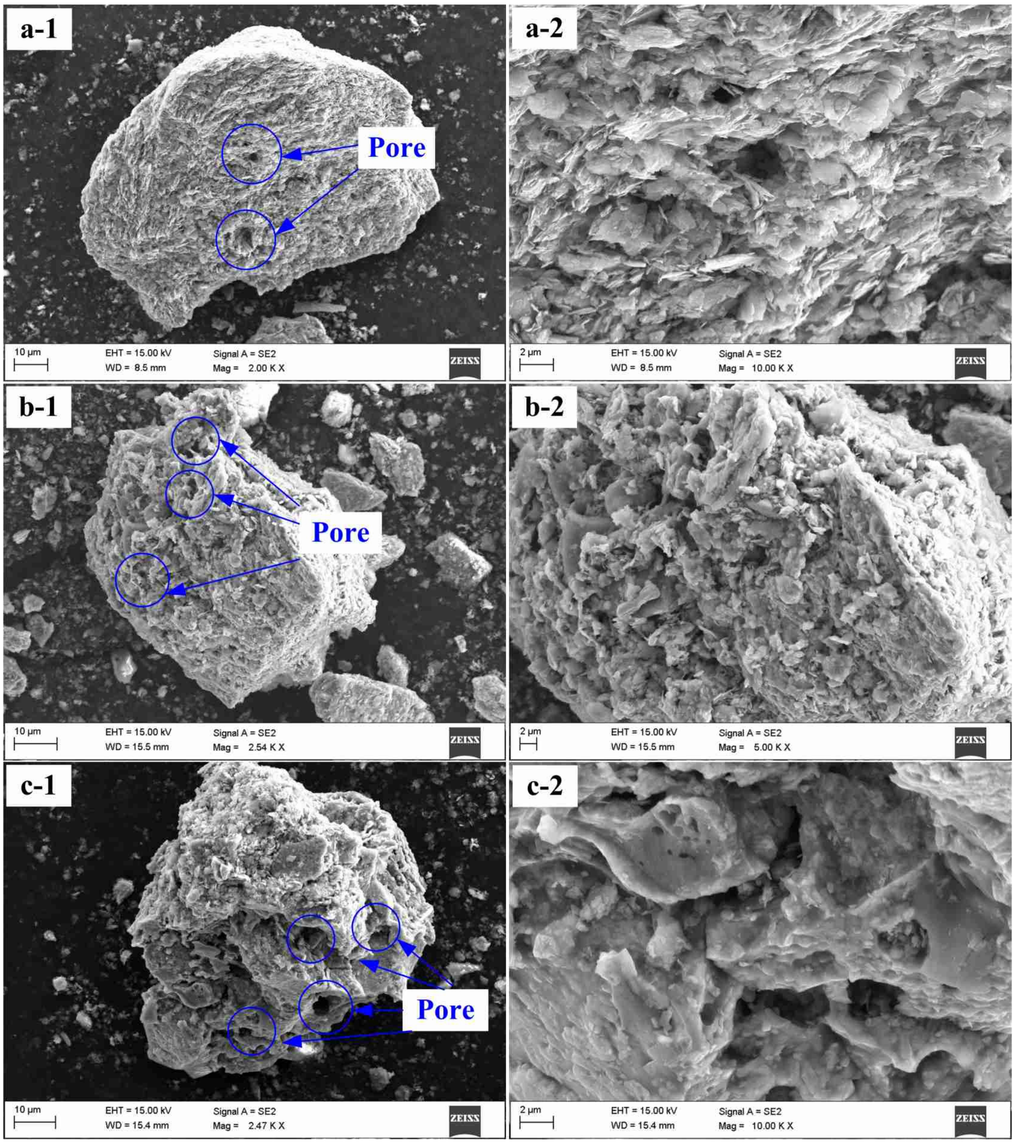

Figure 11. SEM images of materials with different roasting times, with roasting temperature of 650 °C, at a CO concentration of 35%: (**a-1**,**a-2**) 3 min, (**b-1**,**b-2**) 4 min, (**c-1**,**c-2**) 5 min.

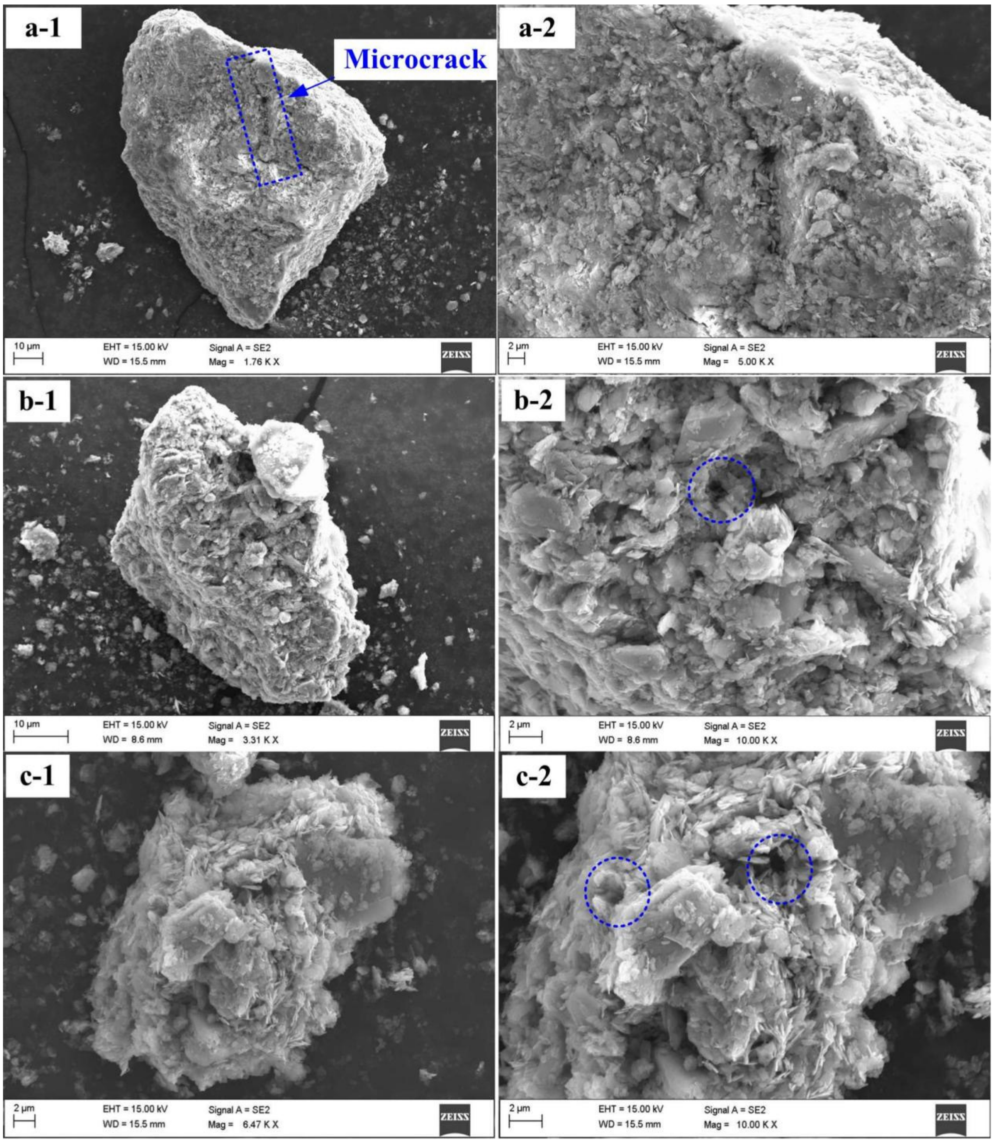

Figure 12. SEM images of materials with different CO contents, with roasting temperature of 650 °C for 5 min: (**a-1**,**a-2**) 15%, (**b-1**,**b-2**) 5%, (**c-1**,**c-2**) 35%.

As shown in Figures 10–12, with the increase of roasting temperature, roasting time, and CO concentration, more pores and pits were formed on the surface of the roasted products, and the particle surface became more loose and rough, showing a fractured and porous structure. Cracks and pores could provide diffusion channels for CO gas during magnetization roasting, so that CO gas could fully contact and react with iron oxide. Therefore, in the process of microwave fluidization magnetization roasting, appropriately increasing the roasting temperature, prolonging the roasting time, and increasing the CO concentration could make the particle surface more loose and rough, produce more cracks and pores, and make the ore surface have honeycomb morphology. This phenomenon was consistent with the research results of other researchers [18–20]. Et tabirou et al. [18] studied the reduction behavior of hematite to magnetite in a CO-CO_2 reducing atmosphere. The results showed that at low temperature (<800 °C), and especially at high CO concentration (>2%), due to the insufficient plasticity (elasticity) of hematite, it was easy to produce microcracks when heated, and the cracks had a high chemical reaction activity. In the process of grain formation and growth of newborn magnetite, due to volume expansion (about 10%), it was also easy to randomly cause microcracks, which further promoted the occurrence of reactions. Therefore, magnetized roasted products are usually porous at low temperature. Another study [20] showed that oolitic hematite ore contained some limonite, siderite, kaolinite, hydroxyapatite, and other minerals containing free water and bound water. The water in these minerals became steam after roasting, resulting in some cracks and pore structures in the ore.

4. Conclusions

The exploration of the microstructure evolution of oolitic hematite during microwave fluidization roasting plays an important role in the study of iron ore reduction mechanisms. The simulation results showed that with the extension of microwave heating time and the increase of microwave power, the overall surface temperature in the particle model increased continuously, and the heating rate of hematite was the fastest, followed by quartz and apatite. Furthermore, the temperature stress and stress difference between the three mineral interfaces in the model increases progressively. The microstructure evolution indicated that there were microcracks between hematite and gangue minerals, such as quartz and apatite, during microwave fluidization roasting, and the microcracks between hematite and quartz minerals were more obvious. With the extension of pretreatment time, microcracks gradually extended and expanded inward along the outer edge of the oolitic, and gradually formed in the core of the oolitic structure. With the increase of roasting temperature, roasting time, and CO concentration, more pores and pits were formed on the surface of the roasted products, and the particle surface presented a loose and rough porous structure.

Author Contributions: Conceptualization, W.Z.; methodology, W.Z.; software, W.Z.; validation, Y.Z.; formal analysis, Y.Z.; investigation, W.Z.; resources, W.Z.; data curation, W.Z., W.G., H.S.; writing—original draft preparation, W.Z.; writing—review and editing, W.Z.; visualization, X.L., C.L.; project administration, W.Z.; funding acquisition, W.Z. All authors have read and agreed to the published version of the manuscript.

Funding: The National Natural Science Foundation of China (Grant No. 52104257), and the start-up fund for talent introduction and scientific research of Shandong University of science and technology (skr21-3-A-022).

Conflicts of Interest: The authors declare no conflict of interest.

References

1. Wu, J.; Wen, Z.J.; Cen, M.J. Development of technologies for high phosphorus oolitic hematite utilization. *Steel Res. Int.* **2011**, *82*, 494–500. [CrossRef]
2. Yu, Y.; Qi, C. Magnetizing roasting mechanism and effective ore dressing process for oolitic hematite ore. *J. Wuhan Univ. Technol. Mater. Sci. Ed.* **2011**, *26*, 176–181. [CrossRef]
3. Xu, C.-Y.; Sun, T.-C.; Kou, J.; Li, Y.-L.; Mo, X.-L.; Tang, L.-G. Mechanism of phosphorus removal in beneficiation of high phosphorous oolitic hematite by direct reduction roasting with dephosphorization agent. *Trans. Nonferrous Met. Soc. China* **2012**, *22*, 2806–2812. [CrossRef]
4. Li, G.; Zhang, S.; Rao, M.; Zhang, Y.; Jiang, T. Effects of sodium salts on reduction roasting and Fe–P separation of high-phosphorus oolitic hematite ore. *Int. J. Miner. Process.* **2013**, *124*, 26–34. [CrossRef]
5. Gao, J.; Guo, L.; Guo, Z. Separation of P Phase and Fe Phase in High Phosphorus Oolitic Iron Ore by Ultrafine Grinding and Gaseous Reduction in a Rotary Furnace. *Met. Mater. Trans. B* **2015**, *46*, 2180–2189. [CrossRef]
6. Jang, K.-O.; Nunna, V.R.M.; Hapugoda, S.; Nguyen, A.V.; Bruckard, W.J. Chemical and mineral transformation of a low grade goethite ore by dehydroxylation, reduction roasting and magnetic separation. *Miner. Eng.* **2014**, *60*, 14–22. [CrossRef]
7. Quast, K. A review on the characterisation and processing of oolitic iron ores. *Miner. Eng.* **2018**, *126*, 89–100. [CrossRef]
8. Dong, Y.B.; Qiang, M.; Duan, Z.Y. Study on the effect of CMS inhibitor on reverse flotation of high phosphorus oolitic hematite in Western Hubei. *Min. Metal. Eng.* **2011**, *31*, 44–47.
9. Li, Y.B.; Gong, W.Q.; Xin, Z.K. Experiment on magnetization roasting and leaching phosphorus removal of a high phosphorus oolitic hematite in Western Hubei. *Met. Mine* **2010**, *5*, 64–67.
10. Li, C.; Sun, H.; Bai, J.; Li, L. Innovative methodology for comprehensive utilization of iron ore tailings: Part 1. The recovery of iron from iron ore tailings using magnetic separation after magnetizing roasting. *J. Hazard. Mater.* **2010**, *174*, 71–77. [CrossRef] [PubMed]

11. Suthers, S.P.; Nunna, V.; Tripathi, A.; Douglas, J.; Hapugoda, S. Experimental study on the beneficiation of low-grade iron ore fines using hydrocyclone desliming, reduction roasting and magnetic separation. *Miner. Process. Extr. Met.* **2014**, *123*, 212–227. [CrossRef]
12. Rath, S.S.; Rao, D.S.; Mishra, B.K. A novel approach for reduction roasting of iron ore slime using cow dung. *Int. J. Miner. Process.* **2016**, *157*, 216–226. [CrossRef]
13. Yu, J.; Han, Y.; Li, Y.; Gao, P. Recent Advances in Magnetization Roasting of Refractory Iron Ores: A Technological Review in the Past Decade. *Miner. Process. Extr. Met. Rev.* **2019**, *41*, 349–359. [CrossRef]
14. Zhou, W.; Sun, Y.; Han, Y.; Gao, P.; Li, Y. Recycling iron from oolitic hematite via microwave fluidization roasting and magnetic separation. *Miner. Eng.* **2021**, *164*, 106851. [CrossRef]
15. Yuan, S.; Zhou, W.; Han, Y.; Li, Y. Efficient enrichment of low-grade refractory rhodochrosite by preconcentration-neutral suspension roasting-magnetic separation process. *Powder Technol.* **2020**, *361*, 529–539. [CrossRef]
16. Severin, J.; Jund, P. Thermal conductivity calculation in anisotropic crystals by molecular dynamics: Application to α-Fe_2O_3. *J. Chem. Phys.* **2017**, *146*, 054505. [CrossRef] [PubMed]
17. Zhang, C.; Li, L.; Yuan, Z.; Xu, X.; Song, Z.; Zhang, Y.R. Mechanical properties of siderite and hematite from DFT calculation. *Miner. Eng.* **2020**, *146*, 106107. [CrossRef]
18. Et-Tabirou, M.; Dupré, B.; Gleitzer, C. Hematite single crystal reduction into magnetite with CO-CO_2. *Mater. Trans. B* **1988**, *19*, 311–317. [CrossRef]
19. Swann, P.R.; Tighe, N.J. High voltage microscopy of the reduction of hematite to magnetite. *Mater. Trans. B* **1977**, *8*, 479–487. [CrossRef]
20. Bahgat, M. Magnetite surface morphology during hematite reduction with CO/CO_2 at 1073 K. *Mater. Lett.* **2007**, *61*, 339–342. [CrossRef]